ACCSCIENCE PUBLISHING

International Journal of Bioprinting

RESEARCH ARTICLE

Black phosphorus scaffolds for efficient bone defect repair via anti-inflammatory, osteogenic, and photothermal therapeutic effects

Peng Xue[1†*], Hongzhong Xi[2†], Wei Zhang[1], Anlong Liu[1], Aoyun Hu[1], Chenjian Peng[1], Jianning Zhao[1*], and Jun Wang[1*]

[1]Department of Orthopedics, Nanjing Hospital of Chinese Medicine Affiliated to Nanjing University of Chinese Medicine, Jiangsu, China

[2]Department of Orthopedics, The Affiliated Hospital of Nanjing University of Chinese Medicine, Nanjing, Jiangsu, China

(This article belongs to the *Special Issue*: *3D Printing for Advancing Orthopedic Applications*)

Abstract

Bone defects pose a high risk of non-union and permanent disability, making effective bone regeneration a critical focus in the development of bone repair materials. Current research primarily emphasizes enhancing the single osteogenic function of bone repair materials, while neglecting the impact of the complex microenvironment in bone defect areas. This has resulted in the failure of many developed bone repair materials to achieve effective *in vivo* bone regeneration. In this study, a multifunctional near-infrared light-responsive black phosphorus (BP) bone repair scaffold was fabricated via low-temperature deposition 3D printing. *In vitro* characterization demonstrated that the scaffold possesses a cancellous bone-like structure, moderate compressive strength, and cytocompatibility, with the ability to promote osteogenesis under inflammatory conditions. *In vivo* studies further confirmed its favorable photothermal responsiveness, enabling photothermal therapy (PTT) to accelerate bone regeneration while reducing inflammation in the defect area. These findings indicate that the multifunctional BP scaffold achieves superior bone repair outcomes through synergistic effects of anti-inflammation, promotion of osteogenic differentiation, and PTT, thereby improving the success rate of defect repair. Moreover, the simple fabrication process and satisfactory therapeutic efficacy of this multifunctional BP scaffold highlight its high potential for clinical translation.

Keywords: Anti-inflammation; Black phosphorus; Bone repair scaffold; Osteogenic differentiation; Photothermal therapy

†These authors contributed equally to this work.

***Corresponding authors:**
Peng Xue (aiwellme@163.com)

Jianning Zhao (zhaojianning.0207@163.com)

Jun Wang (wangjun198607@163.com)

Citation: Xue P, Xi H, Zhang W, *et al*. Black phosphorus scaffolds for efficient bone defect repair via anti-inflammatory, osteogenic, and photothermal therapeutic effects. *Int J Bioprint*. 2026;12(1):586-606. doi: 10.36922/IJB025310310

Received: July 31, 2025
1st revised: August 28, 2025
2nd revised: December 17, 2025
Accepted: December 22, 2025
Published online: December 24, 2025

1. Introduction

Bone defects can result from a variety of factors, including trauma, tumors, and osteonecrosis.[1-3] Failure to adequately repair such defects may lead to persistent pain, pathological fractures, and functional impairment.[4,5] Epidemiological studies have shown that over six million people in China suffer from bone defects or functional disorders

each year, among whom approximately two-thirds require bone grafting treatment. It is projected that by 2050, the costs associated with the treatment of bone defects will exceed 600 billion yuan, imposing a significant burden on patients and society.[6] Autologous bone transplantation, as the gold standard for repairing bone defects, is restricted in its clinical application due to issues such as limited sources and donor site complications.[7] Therefore, the development of artificial bone repair materials has long been a research hotspot in the field of bone tissue engineering.[8] Despite extensive efforts, there is still no widely accepted bone repair material that has successfully transitioned from laboratory research to routine clinical application.

Currently, promoting the proliferation and osteogenic differentiation of bone marrow mesenchymal stem cells (BMSCs) within bone defect areas remains the primary research focus for most bone repair materials. For instance, strategies include incorporating bone repair factors into these materials,[9] loading BMSCs onto them,[10] or engineering material interfaces that are more conducive to BMSC adhesion and proliferation.[11] Despite the promising osteogenic efficacy demonstrated *in vitro*, such scaffolds still fail to achieve satisfactory bone repair outcomes *in vivo*. This discrepancy arises from the intricate microenvironment within *in vivo* bone defects. Under the influence of the complex physiological environment *in vivo*, the robust osteogenic capacity of bone repair materials observed *in vitro* does not guarantee their ability to achieve effective bone repair outcomes *in vivo*. Furthermore, previous research has revealed that under identical intervention conditions, scaffold–host bone integration fails in some experimental animals, compromising the overall success rate of bone repair materials.[12–14] This observation suggests the existence of inter-individual heterogeneity in bone repair responses. These challenges have emerged as significant barriers hindering the translation of bone repair materials from laboratory research to clinical application.

Studies have demonstrated that upon the occurrence of bone defects, the microenvironment at the injured site undergoes significant alterations, primarily characterized by elevated concentrations of hydrogen peroxide and pro-inflammatory factors.[15] These changes impede the expression of osteogenic differentiation transcription factors, thereby inhibiting the differentiation of BMSCs into osteoblasts. Concurrently, the heightened metabolic activity of inflammatory cells (e.g., neutrophils and macrophages) leads to the release of substantial amounts of acidic substances such as lactic acid and carbon dioxide, resulting in a local pH reduction (typically ranging from 5.5 to 6.8, in contrast to the physiological pH of approximately 7.3–7.4 in normal bone tissue).[16] This acidic microenvironment not only hinders normal bone regeneration but may even induce osteolysis. Therefore, excessive levels of pro-inflammatory factors in the bone defect area compromise bone repair through multiple mechanisms. Furthermore, previous clinical studies have revealed inter-individual heterogeneity in bone repair, which is influenced by various risk factors, including age, bone quality, and the use of hormonal medications.[17–19] For patients with delayed bone repair, additional interventions are often required to mitigate the risk of repair failure induced by these factors. Hence, in addition to osteogenesis-promoting properties, bone repair materials need to possess multiple functionalities, including regulating local inflammation in the bone defect area and balancing inter-individual repair heterogeneity through targeted regulatory measures. Such multifunctional materials are more conducive to bone defect healing and enhance the success rate of repair.

Phosphorus is one of the essential elements for bone regeneration, contributing to the maintenance of bone growth and mechanical strength.[20] Black phosphorus (BP), a two-dimensional nanomaterial composed of single phosphorus atoms, exhibits broad-band absorption in the near-infrared (NIR) region and possesses excellent photothermal conversion efficiency.[21] This unique property renders BP a promising photothermal agent, enabling its application in the construction of photothermal nanomaterials for photothermal therapy (PTT). Literature has reported that BP simultaneously exerts both favorable osteogenic and anti-inflammatory effects, thereby facilitating effective bone repair in the bone defect microenvironment.[22] Notably, mild PTT induced by NIR excitation of BP not only promotes osteogenesis and anti-inflammation but also accelerates the release of BP, which in turn enhances its osteogenic and anti-inflammatory efficacy, thereby achieving a synergistic effect.[23] Furthermore, PTT allows for additional regulatory intervention based on individual bone repair status after scaffold implantation, which can accelerate bone healing, balance repair discrepancies caused by inter-individual heterogeneity in bone repair, and prevent repair failure due to delayed bone regeneration. Based on these findings, we intend to develop BP bone repair materials, aiming to fully utilize their multiple functionalities and synergize with PTT to promote bone repair in defect areas, ultimately improving the success rate of bone regeneration.

In the present study, based on our previously developed poly(lactic-co-glycolic acid) (PLGA)/β-tricalcium phosphate (β-TCP) printing paste (composed of β-TCP and PLGA) and low-temperature deposition 3D printing technology,[13] BP/PLGA/β-TCP scaffolds (BP scaffolds) were constructed. The scaffolds were characterized, and their photothermal response properties were examined. Meanwhile, an inflammatory microenvironment was

simulated *in vitro* to assess the osteogenic efficacy of the scaffolds under such conditions. Subsequently, the scaffolds were implanted into a rat model of distal femoral bone defects to investigate their *in vivo* bone repair efficacy under PTT regulation. This study confirmed that BP scaffolds can achieve favorable bone repair outcomes in defect areas through multiple mechanisms, including promoting osteogenic differentiation of BMSCs, regulating local inflammation, and enabling efficient osteogenesis via PTT modulation, thereby exhibiting potential for clinical application.

2. Materials and methods

2.1. Materials

BP nanosheets (Φ100–200 nm) were provided by the College of Engineering, China Pharmaceutical University (Nanjing, China). PLGA and β-TCP powder were purchased from Regenovo Co. (China). Lipopolysaccharides (LPS) were purchased from Yuanye Bio-Technology Co., Ltd. (China). Minimal essential medium Eagle–alpha modification (α-MEM) was purchased from Biological Industries (Israel). Fetal bovine serum, penicillin–streptomycin solution, Live/Dead staining kit, 4',6-diamidino-2-phenylindole (DAPI) staining kit, Alizarin red S (ARS) staining kit, and alkaline phosphatase (ALP) staining kit were purchased from Beyotime Biotechnology (China). Enzyme-linked immunosorbent assay (ELISA) kits (bone morphogenetic protein 2 [BMP-2], ALP, runt-related transcription factor 2 [RUNX2], osteocalcin [OCN]) were purchased from Jingren Medical Research (China). BMP-2 (66383-1-Ig), tumor necrosis factor-alpha (TNF-α; [17590-1-AP, and cluster of differentiation 86 (CD86; 26903-1-AP)]) antibodies were purchased from Proteintech Biotechnology Co., Ltd. (China). ALP (sc-365765), RUNX2 (sc-101145), OCN(sc-73464), and β-actin (sc-517582) antibodies were purchased from Santa Cruz Biotechnology (United States of America [USA]). Hematoxylin and eosin (H&E) and Masson staining kits were purchased from Ai Fang Bio Co. (China).

2.2. Preparation of black phosphorus scaffold

According to a published research protocol,[13] a mixture was prepared by dispersing 10 g of PLGA granules and 2.5 g of β-TCP in 42 mL of a 1,4-dioxane solution using vortex shaking for 1 min, followed by magnetic stirring until a homogeneous solution was obtained. Various ratios of BP (0%, 0.5%, 1%, and 2%) were added to the solution and stirred again. The resulting BP-doped slurry was then transferred to a printing cylinder equipped with a piston and a needle of appropriate size (Φ0.25 mm) and loaded onto a biological 3D printer (Regenovo Co.). After printing, the scaffolds were pre-cooled in a refrigerator at −80°C for 2 h, freeze-dried for 24 h, and stored at −20°C for future use. The resulting scaffolds were named BP scaffolds and classified as 0BP, 0.5BP, 1BP, and 2BP according to the BP doping amount.

2.3. Characterization of black phosphorus scaffold

The characterization of the scaffolds was based on a previously reported research protocol. Specifically, scanning electron microscopy (SEM; Apreo 2, Thermo Fisher Scientific, USA), atomic force microscopy (Hyperion II System, Thermo Fisher Scientific, USA), and energy-dispersive X-ray spectroscopy (EDS; Dual-X Super-X EDS System, Thermo Fisher Scientific, USA), Fourier transform infrared spectroscopy (FTIR; Nicolet iS50, Thermo Fisher Scientific, USA), X-ray photoelectron spectroscopy (XPS; Escalab 250Xi, Thermo Fisher Scientific, USA), and X-ray diffraction (D8 VENTURE, Bruker, Germany). The compressive strength was measured using a universal mechanical tester (Shenzhen SUNS, China). The porosity and pore diameter of the scaffolds were calculated using the software (Bio Architect) provided by the printing company (Regenovo Co.).

2.4. Analysis of the photothermal performance of the scaffolds

An 808 nm NIR laser (New Industries Optoelectronics Technology Co., Ltd., China) with a power of 0.8 W/cm^2 was used to irradiate different scaffolds for 300 s, and the temperature was recorded. Infrared images were captured using an infrared thermal camera (Model: H23, Hikmicrotech Co., Ltd., China), and the temperatures were quantified to plot temperature rise curves. The temperature trends of different scaffolds under 808 nm NIR laser irradiation at 0.8 W/cm^2 were obtained.

The 2BP scaffolds were irradiated with an 808 nm NIR laser at different power densities (0.6, 0.7, 0.8, 0.9, and 1.0 W/cm^2), and the temperature changes were recorded and plotted.

An 808 nm NIR laser at 0.8 W/cm^2 was used to irradiate the BP scaffolds for 300 s, and the endpoint temperatures were recorded. The process was repeated 10 times.

2.5. Cytotoxicity analysis

2.5.1. Cell culture

Rat BMSCs and RAW 264.7 cells were purchased from the Shanghai Cell Bank of the Chinese Academy of Sciences (China) and cultured in α-MEM complete medium containing 10% fetal bovine serum and 1% penicillin–streptomycin. Cells were maintained at 37°C in a humidified atmosphere with 5% carbon dioxide. The medium was changed every 2 days. Cells were passaged under an inverted microscope (Model, Olympus, Japan)

at 80%–90% confluence, and passage 3 cells were used for subsequent experiments. Unless otherwise specified, the NIR irradiation conditions were as follows: 808 nm, 0.8 W/cm^2, 5 min per day.

2.5.2. Cytotoxicity

Leaching solutions were prepared according to previously reported methods. Briefly, the scaffolds were rinsed with phosphate-buffered saline (PBS), sterilized with ethylene oxide, and placed in extraction vessels. The leaching solutions were prepared at a concentration of 0.2 g/mL in complete medium and incubated at 37°C for 72 h.

For the Cell Counting Kit-8 (CCK-8) assay, BMSCs were seeded into 96-well plates at a density of 1000 cells/well. Subsequently, 100 μL of the different leaching solutions was added to each well, and the medium was refreshed every 24 h. After incubation for 1, 3, and 5 days, the medium was discarded, and 100 μL of α-MEM containing 10% CCK-8 solution was added to each well, followed by an additional 2 h of incubation. The absorbance at 450 nm (A450) was measured using a microplate reader (BioTek, USA).

For Live/Dead staining, cells were cultured under the same conditions as described above, with 2000 cells seeded per well. Live/Dead staining was performed according to the instructions of the calcein acetoxymethyl and propidium iodide staining kit. Images were captured using an inverted fluorescence microscope (Olympus, Japan), where green fluorescence represents live cells and red fluorescence indicates dead cells.

2.5.3. Co-culture of cells and scaffolds

Cell growth on different scaffolds was observed by nuclear staining. Cells were seeded on the scaffolds at a density of 1×10^4 cells/well, and the medium was removed after 24 h of co-culture. Cells were then fixed with paraformaldehyde for 5 min and rinsed with PBS for 10 min. Subsequently, 0.5% TritonX-100 was added and incubated for 20 min. The nuclei were stained with the DAPI (blue) staining kit according to the manufacturer's instructions. Images were captured using an inverted fluorescence microscope (Olympus, Japan).

2.6. Osteogenic induction under an inflammation-free microenvironment

BMSCs were inoculated into 12-well plates at a density of 3×10^4 cells/well and incubated. When cell confluence reached 80%–90%, scaffolds that had been immersed in complete medium for 30 min were placed into the 12-well plates. Subsequently, osteogenic induction medium was added (50 mg/L ascorbic acid, 10 mmol/L β-glycerophosphate, and 100 nmol/L dexamethasone) and changed every 2 days. ALP and ARS staining was performed according to the manufacturer's instructions after 6 days and 14 days of incubation, respectively. After termination of the reactions, the staining results were observed under an inverted microscope (Olympus, Japan). Six regions of interest were randomly selected for quantitative analysis of positive staining areas using ImageJ (version 1.54r, Developer: Wayne Rasband, National Institutes of Health, USA).

2.7. Photothermal therapy-enhanced bone repair efficacy of scaffolds

The 0BP scaffolds were used as the control group, and the 2BP scaffolds were used as the experimental group. The groups were further subdivided into PTT and non-PTT groups according to whether NIR irradiation (808 nm, 0.8 W/cm^2) was applied at a frequency of 5 min/day. To observe more pronounced *in vitro* osteogenic effects, ALP and ARS staining were performed on days 9 and 21 of osteogenic induction, respectively. All other cell culture procedures, data collection, and analysis steps were conducted as described above.

2.8. Molecular mechanisms underlying scaffold-promoted bone repair

2.8.1. Western blotting

Scaffolds were co-cultured with the cells for 5 days to analyze the expression of osteogenesis-related proteins in BMSCs. Cells on the scaffold and in the culture dishes were lysed by adding 200 μL of lysis buffer and incubated for 20 min. After centrifugation at 12,000 rpm for 20 min, the precipitate was discarded, and the protein concentration in the supernatant was determined using a bicinchoninic acid protein assay kit. Protein samples were separated by sodium dodecyl sulfate–polyacrylamide gel electrophoresis and transferred onto polyvinylidene fluoride membranes. The membranes were blocked with 5% skimmed milk for 2 h and then incubated overnight at 4°C with BMP-2 (1:500), RUNX2 (1:800), ALP (1:500), OCN (1:1000), and β-actin (1:5000). Subsequently, the membranes were incubated with secondary antibodies (1:3000) for 1 h at room temperature. Target protein bands were detected using a chemiluminescent imaging system (Bio-Rad, USA).

2.8.2. Enzyme-linked immunosorbent assay

Cellular proteins were extracted using the same method as described above. The levels of BMP-2, RUNX2, ALP, and OCN in the protein samples were quantified and statistically analyzed according to the ELISA instructions.

2.9. Osteogenic induction under an inflammatory microenvironment

The osteogenic induction medium was prepared under an inflammatory microenvironment according to previously reported methods. RAW 264.7 cells were seeded in 12-well

plates at a density of 5×10^5/well, and the culture medium was collected after 24 h of co-culture. After centrifugation, the supernatant was mixed with osteogenic induction medium at a volume ratio of 1:2 to obtain inflammatory osteogenic induction medium. According to the experimental groups (control, LPS, LPS+0BP, LPS+2BP, and LPS+2BP+NIR), BP scaffolds (0BP or 2BP) pre-immersed in complete medium for 30 min were placed into 12-well plates for co-culture with BMSCs. NIR irradiation frequency and other experimental procedures were performed as described above. After 14 days of osteogenic induction, ALP staining was conducted to evaluate osteogenic differentiation.

2.10. Anti-inflammatory mechanism of black phosphorus scaffolds

RAW 264.7 cells were seeded in 12-well plates at a density of 5×10^5/well. After LPS induction, the cells were co-cultured with different BP scaffolds for 48 h and subjected to NIR irradiation according to the group design (LPS+0BP, LPS+2BP, and LPS+2BP+NIR). CD86 immunofluorescence staining was performed following the cytotoxicity assay. The culture medium was discarded, and the cells were washed with PBS for 5 min. Cells were fixed with 4% paraformaldehyde for 15 min and washed three times with PBS for 5 min each. Subsequently, cells were permeabilized with 2 mL of 0.5% Triton X-100 for 10 min and washed with PBS. Blocking was performed using 2% goat serum for 30 min. Cells were then incubated with fluorescent primary antibodies against CD86 for 1 h at room temperature, washed with PBS, and incubated with fluorescent secondary antibodies for 40 min. After washing three times with PBS, DAPI was added for 5 min to stain the nuclei. After final washing (three times), images were captured using an inverted fluorescence microscope (Olympus, Japan). Western blotting was conducted as described in **Section 2.8.1**.

Total RNA was extracted and sequenced on an Illumina NovaSeq 6000 platform (PE150; Illumina, USA). Clean reads were aligned to the rat reference genome (mRatBN7.2) using HISAT2 (v2.0.4). Transcript assembly and fragments per kilobase million quantification were performed using StringTie (v1.3.0). Differentially expressed genes (DEGs) between the 0BP and 2BP groups were identified using edgeR, with thresholds of $|\log_2 FC| \geq 1$ and Q-value ≤ 0.05. Functional enrichment analysis of DEGs was conducted using DAVID. Selected DEGs were validated by quantitative polymerase chain reaction (qPCR) using gene-specific primers (**Table S1**). Complementary DNA was synthesized from total RNA, and qPCR reactions were performed using SYBR Green (Bio-Rad Laboratories, USA). Gene expression levels were normalized to *Gapdh* and calculated using the $2^{-\Delta\Delta Ct}$ method, with six biological replicates ($n = 6$). Statistical significance was assessed using Student's t-test ($p < 0.05$).

2.11. Animal feeding and modeling

2.11.1. Animal husbandry

This study was approved by the Ethics Committee of the Affiliated Hospital of Nanjing University (Approval No. 2025 DW-002-01). Thirty Sprague–Dawley male rats (200 ± 10 g; Jiangsu Qinglongshan Biotechnology Co., Ltd., China) were housed at 24–26°C. All animals were humanely cared for in accordance with the Guide for the Care and Use of Laboratory Animals.

2.11.2. Bone defect modeling and scaffold implantation

After anesthesia, the surgical area was prepared with the lateral femoral condyle as the center. A 1 cm incision was made to expose the femoral shaft, centered on the lateral femoral condyle. The skin, fascia, and muscle were incised layer by layer to expose the lateral side of the knee joint. A bone tunnel with a diameter of 3 mm was drilled in the center of the lateral femoral condyle using a handheld electric drill. The scaffold was then implanted into the bone defect area, and the incision was closed in layers and sterilized with iodine. 3 days postoperatively, 200,000 units of penicillin were administered intramuscularly daily to prevent infection, and incision healing and the animals' condition were monitored.

2.12. Evaluation of the near-infrared response of the scaffold *in vivo*

After surgery, anesthetized rats were irradiated with NIR light (808 nm, 1.2 W/cm^2, 10 min) once per week. An infrared thermal camera was utilized to capture photothermal images, and the corresponding temperature variations were monitored.

2.13. Evaluation of scaffolds for bone repair *in vivo*

2.13.1. Specimen collection

Animals were euthanized at 6 weeks postoperatively to collect the distal femur on the operated side for evaluation of bone repair. Major organs, including the heart, liver, spleen, lungs, and kidneys, were also collected for safety analysis.

2.13.2. Radiological evaluation

Bone regeneration within the defect area was assessed using high-resolution micro-computed tomography (Siemens, Germany) with the following parameters: 80 kV voltage, tube current of 500 μA, and a pixel resolution of 40.5 μm. Reconstructed images in sagittal, coronal, and horizontal planes were acquired, and bone quality within the defect area was quantified using trabecular thickness,

trabecular number, bone mineral density, and bone volume/total volume.

2.13.3. Histological evaluation

After fixation in 4% paraformaldehyde, bone tissue specimens were completely decalcified in 10% ethylenediaminetetraacetic acid and dehydrated in ethanol. The samples were then embedded in paraffin, and 6 μm-thick sections were prepared for histological and immunohistochemical analysis. H&E, Masson's trichrome, BMP-2, and CD86 staining were performed according to the manufacturers' instructions. The stained sections were examined using a light microscope (Model, Nikon, Japan). Image J software was used to evaluate positively stained areas for semi-quantitative analysis.

2.14. *In vivo* biocompatibility analysis

H&E staining of major organs was performed to assess the presence of pathological changes.

2.15. Statistical analysis

All data are expressed as the mean ± standard deviation. Statistical analyses were performed using analysis of variance followed by Tukey's post hoc test unless otherwise stated. A value of $p < 0.05$ was considered statistically significant ($^{*}p < 0.05$, $^{**}p < 0.01$, $^{***}p < 0.001$) while $p > 0.05$ was considered non-different (ns). Statistical analyses were performed using SPSS 22.0 software (IBM, USA).

3. Results and discussion

3.1. Morphological and chemical characteristics of black phosphorus scaffolds

Figure 1A presents digital images of BP scaffolds with varying mass ratios of BP, all of which exhibit regular, permeable, and porous structures. Given that BP is a black powder, the scaffold without BP incorporation appears milky white, while BP-containing scaffolds generally display a darker color, with uniformly distributed BP visible throughout the scaffolds (indicated by red arrows). The color intensity of the scaffolds gradually deepens with increasing BP content. Notably, excessive BP incorporation leads to clogging of the printing nozzle, hindering scaffold fabrication. After multiple optimizations, a BP mass ratio of 2% was determined to be the maximum feasible concentration. SEM images (Figure 1B) reveal that the scaffold struts are regularly shaped with slight surface curvature. High-magnification SEM images further demonstrate the complex, hierarchical porous structures characteristic of low-temperature deposition technology, which facilitate substance metabolism and exchange, as well as cellular infiltration into the scaffold interior, enabling creeping substitution. Importantly, these porous structures are consistently observed across all scaffolds, indicating that BP incorporation does not alter the scaffold microstructure. Atomic force microscopy further confirms the porous structure morphology and verifies that BP incorporation does not affect the scaffold microstructure (Figure 1C). EDS was employed to analyze phosphorus elemental variations in BP scaffolds. As BP consists solely of phosphorus, changes among the scaffolds were primarily reflected in the phosphorus content. With increasing BP ratio, phosphorus content exhibited a positive correlation with BP incorporation, while the proportions of other elements showed only minor, non-significant fluctuations (Figure 1D).

Figure 1E displays the FTIR spectra of the blank scaffold (0BP), and Figure 1F presents the spectra of the scaffold containing 2% BP (2BP). The primary components of the 0BP scaffold are β-TCP and PLGA. Characteristic absorption peaks at 1750 cm^{-1} and 1080 cm^{-1} correspond to the C=O and C–O bonds of PLGA, respectively. Peaks at 1453 cm^{-1}, 1381 cm^{-1}, 1266 cm^{-1}, and 1190 cm^{-1} are associated with the rocking and bending vibrations of CH_2 and CH_3 groups in PLGA.[24] Absorption peaks in the range of 543–605 cm^{-1} are attributed to the bending vibrations of PO_4^{3-} groups in β-TCP (Figure 1D, black curve).[25,26] Due to the extremely low BP content and overlapping FTIR bands of β-TCP and BP, no distinct spectral differences were observed after BP addition (Figure 1F, black curve).[27] Additionally, Figure 1E and F presents the FTIR spectra of scaffolds immersed in simulated body fluid for 3 days (red curve), 7 days (blue curve), 14 days (green curve), 21 days (purple curve), and 28 days (yellow curve). No significant spectral changes were observed for either 0BP or 2BP over time, indicating minimal chemical alteration or degradation of the scaffolds. These results suggest that the scaffolds possess excellent stability and can maintain their structural and physical properties over the examined period. Figure S1A shows the X-ray diffraction patterns of 0BP and 2BP scaffolds. No obvious differences were observed between the two groups, and the diffraction peaks correspond well with those of tricalcium phosphate ($Ca_3(PO_4)_2$, PDF#86-1585), with characteristic peaks at $2\theta = 30.94°$ and 34.14°. To further confirm the presence of BP in the scaffolds, XPS was conducted to analyze the surface chemical composition. As shown in the XPS survey spectrum (Figure S1B), the phosphorus (P2p) signal is detectable, although relatively weak due to low BP content. High-resolution P2p spectra clearly confirm the presence of phosphorus in the 0.5BP, 1BP, and 2BP scaffolds (Figure S1C), consistent with the EDS results. Collectively, these findings confirm the successful fabrication of BP scaffolds.

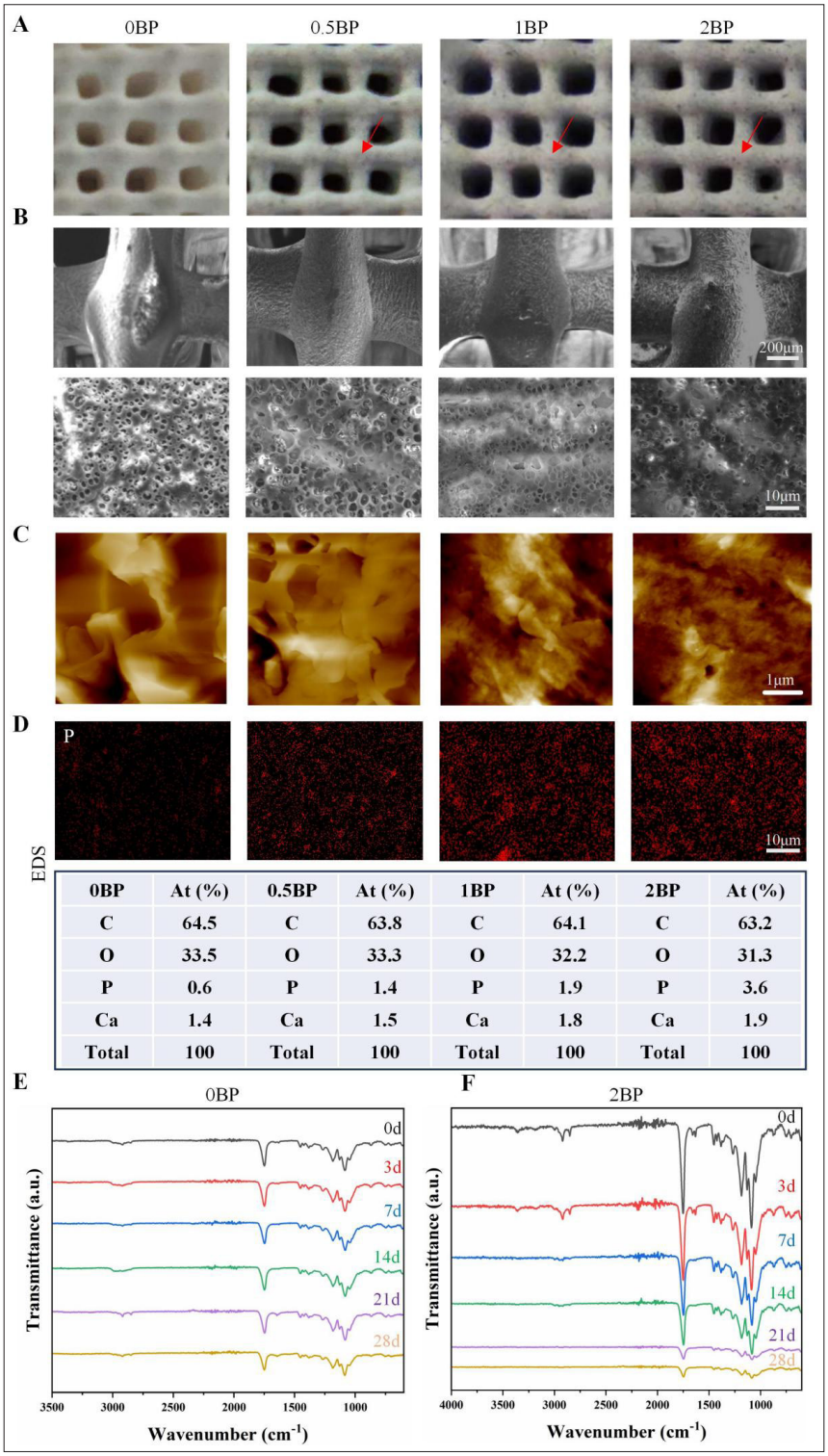

0BP	At (%)	0.5BP	At (%)	1BP	At (%)	2BP	At (%)
C	64.5	C	63.8	C	64.1	C	63.2
O	33.5	O	33.3	O	32.2	O	31.3
P	0.6	P	1.4	P	1.9	P	3.6
Ca	1.4	Ca	1.5	Ca	1.8	Ca	1.9
Total	100	Total	100	Total	100	Total	100

Figure 1. Morphology and characterization of BP scaffolds. (A) Top views of scaffolds with different BP contents captured using a digital camera. (B) Scanning electron microscopy images of the scaffolds at different magnifications (scale bars: 200 μm [top row] and 10 μm [bottom row]; magnifications: 60× [top row] and 1000× [bottom row]). (C) Atomic force microscopy images of scaffolds (scale bar: 1 μm; magnification: 2000×). (D) Elemental surface analysis of different scaffolds (scale bar: 10 μm; magnification: 1000×). Fourier transform infrared spectra of (E) 0BP and (F) 2BP scaffolds after immersion in simulated body fluid for 0, 3, 7, 14, 21, and 28 days (d). 0BP, 0.5BP, 1BP, and 2BP represent scaffolds containing 0%, 0.5%, 1%, and 2% BP by mass, respectively. Abbreviations: BP, black phosphorus; EDS, energy-dispersive X-ray spectroscopy.v

3.2. Physical characteristics and *in vitro* photothermal performance of black phosphorus scaffolds

As scaffolds for bone tissue engineering, appropriate porosity and compressive strength are crucial for supporting bone regeneration. Figure 2A and B demonstrates that the fabricated scaffolds exhibited a porosity of 75 ± 3% and a compressive strength of 2.5±0.2 MPa. These parameters fall within the commonly accepted range in bone tissue engineering for mimicking the mechanical and structural properties of cancellous bone.[13] These architectural features are critical for facilitating nutrient exchange, cellular infiltration, and ultimately, the formation of new bone tissue within the defect site. In addition to structural suitability, adequate mechanical strength is pivotal for maintaining stability at the defect area during the early stages of bone healing. Figure 2C shows that scaffolds initially exhibited compressive strength comparable to that of cancellous bone, enabling effective mechanical support immediately after implantation. Although a gradual decrease in compressive strength was observed during degradation, the scaffolds retained most of their mechanical integrity within 4 weeks, ensuring sufficient support during the critical early phase of bone regeneration. Subsequently, the *in vitro* photothermal performance of BP scaffolds was evaluated. Figure 2D illustrates the temperature changes of different scaffolds under NIR irradiation at a constant power. All BP scaffolds exhibited excellent photothermal responsiveness, characterized by a rapid temperature increase within 5 s, followed by a stable plateau. This rapid and stable heating profile is advantageous for achieving controlled thermal stimulation in a timely manner.

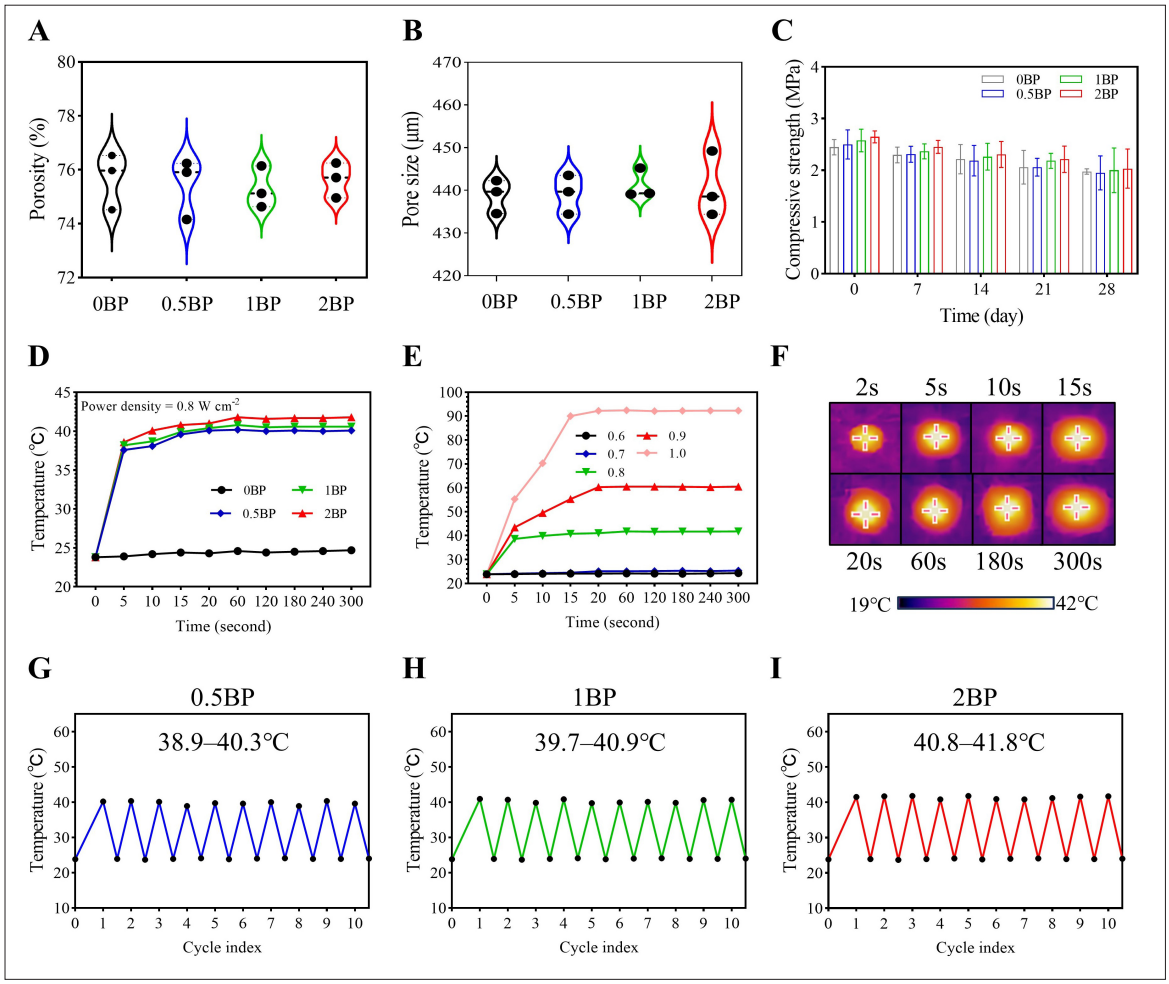

Figure 2. Characterization and photothermal response of black phosphorus (BP) scaffolds. (A) Porosity, (B) pore size, and (C) compressive strength of the scaffolds over time. (D) Temperature rise curves of different scaffolds under near-infrared (NIR) irradiation (808 nm, 0.8 W/cm^2). (E) Temperature rise curves of 2BP under NIR irradiation at different power densities (808 nm, 0.6–1.0 W/cm^2). (F) Infrared thermal images of 2BP under NIR irradiation (808 nm, 0.8 W/cm^2). (G–I) Cyclic photothermal performance of different scaffolds. 0BP, 0.5BP, 1BP, and 2BP represent scaffolds containing 0%, 0.5%, 1%, and 2% BP by mass, respectively.

To optimize the NIR power density, the temperature response of the 2BP under varying NIR power densities was further investigated (Figure 2E). At 0.6 W/cm^2, negligible temperature changes were observed, indicating that a threshold power density is required to trigger effective photothermal conversion. As the power density increased, both photothermal response efficiency and scaffold temperature rose accordingly, with irradiation at 1.0 W/cm^2 resulting in a stable high temperature exceeding 90°C. However, such extreme temperatures pose a risk of thermal damage to surrounding cells and tissues, underscoring the need to identify an optimal power density that balances therapeutic efficacy and biocompatibility. Notably, numerous studies have reported that PTT induced by mild thermal stimulation (40–42°C) promotes BMSC proliferation and osteogenic differentiation, enhances ALP activity, and accelerates mineralization—key processes in effective bone regeneration.[28] Under 0.8 W/cm NIR irradiation, the 2BP scaffold demonstrated efficient photothermal conversion, with the temperature stabilizing within the optimal range (40–42°C) within 5 s (Figure 2E). This observation was further corroborated by infrared thermal images acquired at different time points, which confirmed stable maintenance of mild hyperthermia (Figure 2F). For *in vivo* applications, repeated NIR-irradiation is often required to sustain therapeutic effects, necessitating stable photothermal performance over multiple cycles. Figure 2G–I shows that the 2BP maintained consistent photothermal conversion efficiency over 10 NIR irradiation cycles, ensuring its suitability for repeated therapeutic interventions.

Collectively, these results demonstrate that the BP scaffolds possess favorable physical properties, including appropriate porosity, pore size, and mechanical strength, as well as efficient photothermal conversion capability. Under the optimized NIR power density (0.8 W/cm^2), the scaffolds can generate controlled mild thermal stimulation (40–42°C), which is expected to synergistically enhance bone regeneration by modulating cellular activities while providing structural support. This combination of structural and functional attributes establishes a solid foundation for potential applications in bone defect repair.

3.3. Cytotoxicity and osteogenic induction under an inflammation-free microenvironment *in vitro*

For scaffolds intended for *in vivo* implantation, non-cytotoxicity is a fundamental prerequisite to ensure biocompatibility and avoid adverse host responses. Rat BMSCs were selected as the model cells to evaluate the cytocompatibility of BP scaffolds (Figure 3). Live/Dead staining after co-culture (Figure 3A) revealed minimal red-stained dead cells at all-time points, with extensive green-stained viable cells uniformly distributed, confirming the non-cytotoxic nature of the scaffolds. Consistent with these observations, CCK-8 assays (Figure 3E) demonstrated robust proliferation of BMSCs in all groups over time, further validating the excellent cytocompatibility of the scaffolds. Additionally, nuclear staining of cells co-cultured with scaffolds for 24 h revealed abundant cell adhesion on the scaffold surfaces (Figure 3B), indicating that the scaffolds provide a favorable microenvironment for initial cell attachment. This initial adhesion is a critical step for subsequent cellular processes such as proliferation and differentiation. To determine the optimal BP mass ratio for enhancing osteogenesis, osteogenic induction assays were performed. BMSCs were co-cultured with scaffolds in osteogenic induction medium, and ALP staining was conducted to assess early osteogenic differentiation, as ALP is a key marker enzyme of mature osteoblasts and directly reflects the extent of BMSC osteogenic commitment.[29] The ALP staining results (Figure 3C) showed that the positively stained area increased with increasing BP mass ratios, with statistically significant differences observed among groups (Figure 3F). These results indicate that BP scaffolds promote BMSC osteogenic differentiation in a dose-dependent manner within the tested range, with the 2BP exhibiting the strongest effect. ARS staining was further employed to evaluate late-stage osteogenic mineralization, as calcium nodule formation by osteoblasts represents a terminal marker of mineral deposition. As shown in Figure 3D and **G**, BP scaffolds significantly enhanced mineralization compared to the control, and a higher BP content was associated with increased mineral nodule formation. Collectively, these findings demonstrate that BP scaffolds exhibit excellent biocompatibility (non-cytotoxicity) and significantly promote BMSC osteogenic differentiation and mineralization under inflammation-free conditions. Among the tested formulations, the 2BP scaffold showed the most pronounced osteogenic effect, supporting its selection for subsequent *in vitro* and *in vivo* studies.

3.4. The promotional effect and mechanism of photothermal therapy on osteogenesis of black phosphorus scaffolds

Building upon the above preliminary screening, 2BP was identified as the optimal formulation and was therefore selected for subsequent investigations into the effect of mild PTT (40–42°C) induced by NIR irradiation on osteogenesis. The study design included a control group (0BP) and an experimental group (2BP), with additional NIR-irradiated subgroups to evaluate photothermal-mediated effects. In the absence of NIR stimulation, 2BP already exhibited superior osteogenic potential compared with 0BP, as evidenced by more intense ALP staining and larger areas of mineralized nodules in ARS staining

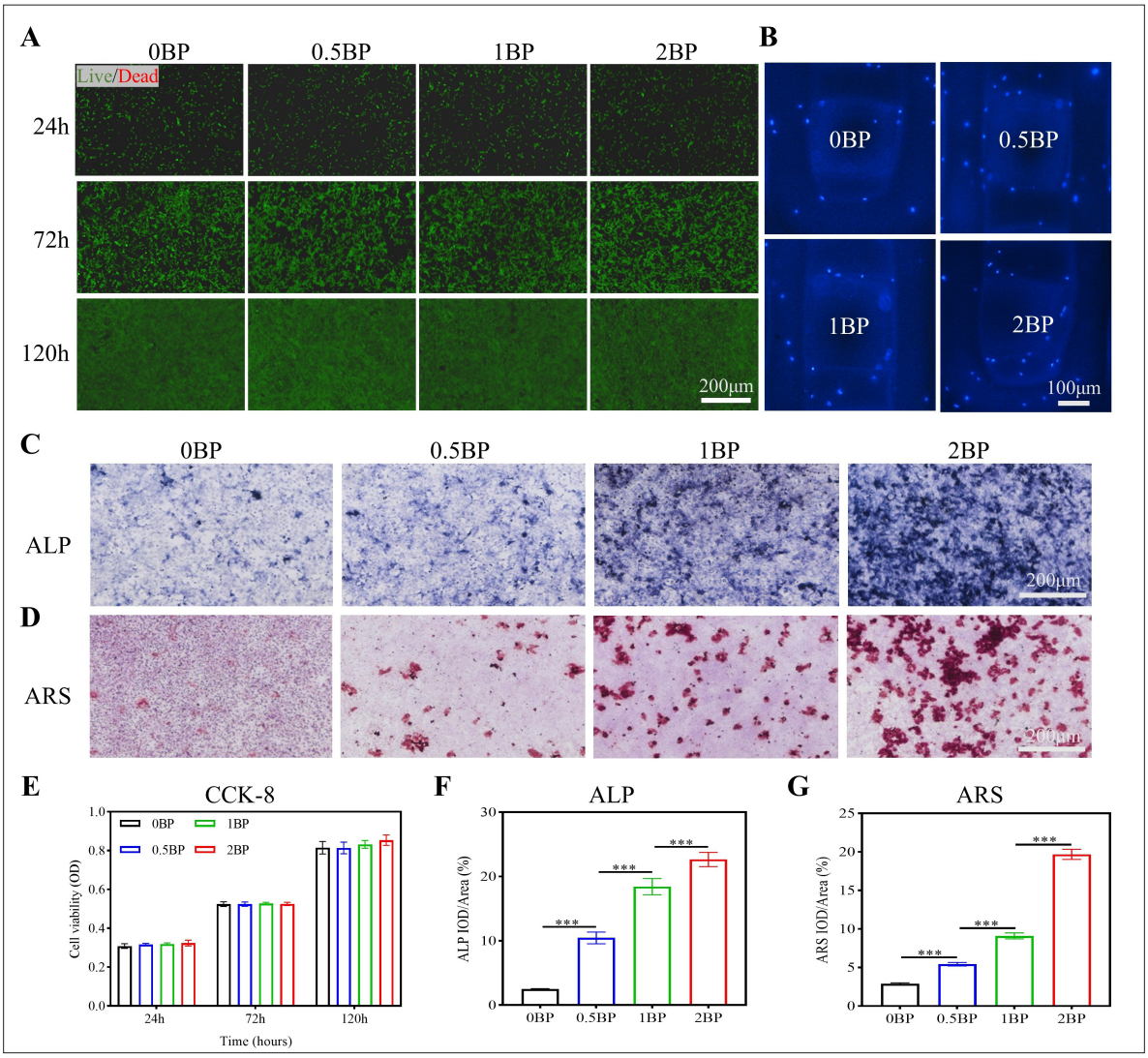

Figure 3. Biocompatibility and osteogenic capacity of black phosphorus (BP) scaffolds. (A) Live/Dead staining of bone marrow mesenchymal stem cells (BMSCs) cultured in scaffold leaching solutions (scale bar: 200 μm; magnification: 40×). (B) Nuclear staining of BMSCs on scaffold surfaces (scale bar: 100 μm; magnification: 40×). (C) alkaline phosphatase (ALP) staining after 6 days of co-culture and (D) Alizarin red S (ARS) staining after 14 days of co-culture (scale bar: 200 μm; magnification: 40×). (E) Cell Counting Kit-8 (CCK-8) assay of BMSCs cultured in scaffold leaching solutions. (F) Semi-quantitative analysis of ALP staining. (G) Semi-quantitative analysis of ARS staining. $n = 6$; ns = $p > 0.05$, *** $p < 0.001$. 0BP, 0.5BP, 1BP, and 2BP represent scaffolds containing 0%, 0.5%, 1%, and 2% BP by mass, respectively.

(Figure 4A & B). Upon NIR irradiation, the 2BP+NIR group showed the most robust osteogenic induction among all groups, with maximal positive expression in both ALP and ARS staining under the same induction period. In contrast, NIR irradiation failed to enhance osteogenesis in the 0BP group, which can be attributed to the lack of BP—a critical photothermal converter—resulting in the inability to generate the requisite mild hyperthermia for PTT.

To explore the underlying mechanism by which 2BP promotes BMSC osteogenic differentiation, an ELISA was performed. The results revealed that the 2BP upregulated the expression of key osteogenic proteins, including BMP-2, RUNX2, ALP, and OCN, with further enhancement observed upon NIR irradiation (Figure 4C). These proteins play pivotal roles in orchestrating osteogenic differentiation and bone maturation: BMP-2 initiates the osteogenic cascade, RUNX2 acts as a master transcription factor regulating osteoblast commitment, ALP mediates early mineralization, and OCN is a late marker of osteoblast maturation, collectively contributing to bone regeneration. The synergistic effect of NIR irradiation is likely dual-faceted: NIR not only accelerates BP degradation to release bioactive phosphorus ions but also provides mild

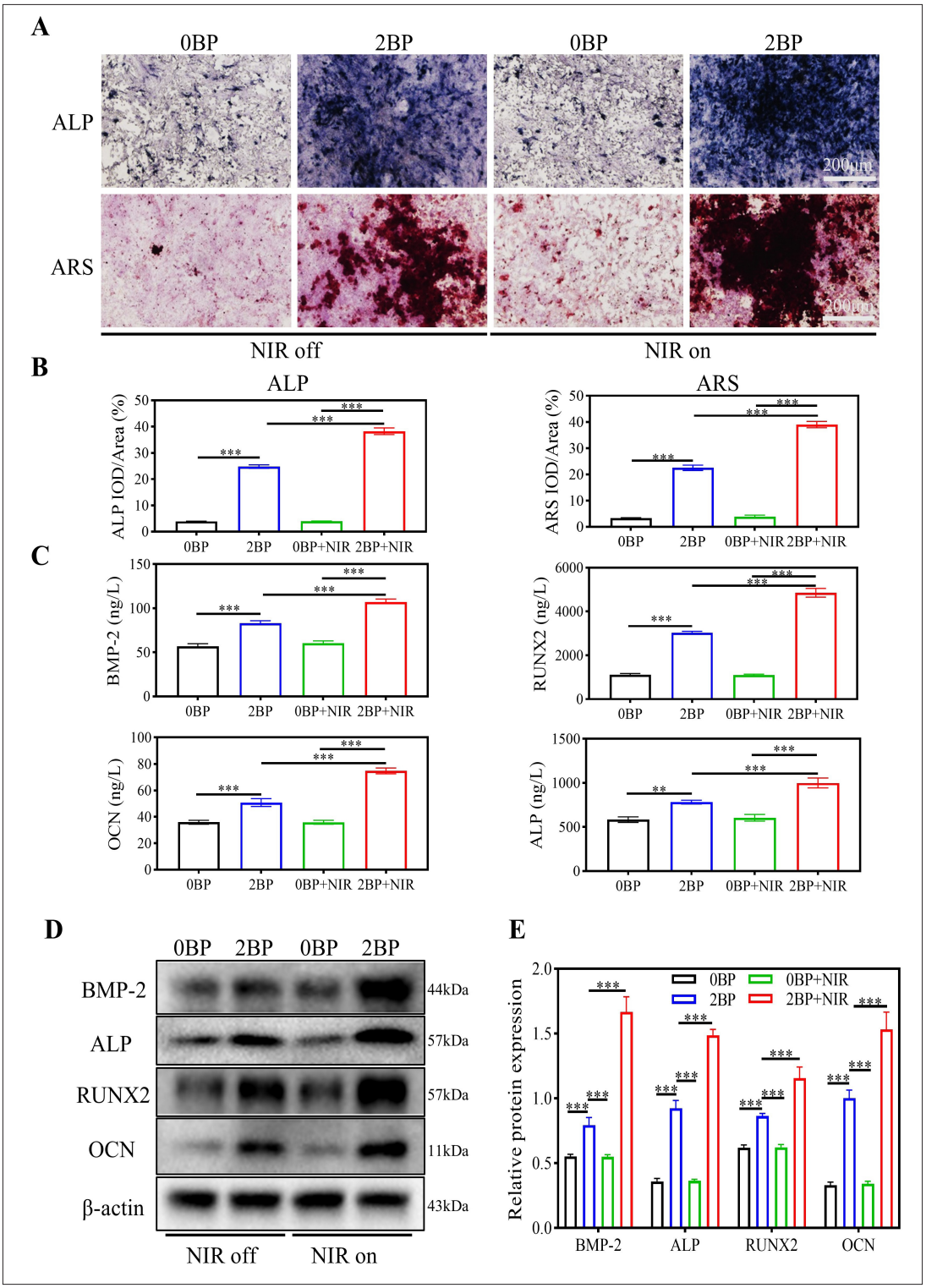

Figure 4. Evaluation of PTT-promoted scaffolds for *in vitro* osteogenesis. (A) ALP staining after cells were co-cultured with scaffolds for 9 days and ARS staining at 21 days (scale bar: 200 μm; magnification: 40×). (B) Semi-quantitative analysis of ALP and ARS staining. (C) Enzyme-linked immunosorbent assay after co-culture of scaffolds with BMSCs. (D) WB after co-culture of scaffolds with BMSCs. (E) Semi-quantitative analysis of WB. Notes: NIR parameters: 808 nm, 0.8 W/cm^2, 5 min per day. $n = 6$, $^*p < 0.05$, $^{**}p < 0.01$, $^{***}p < 0.001$. 0BP and 2BP represent scaffolds containing 0% and 2% BP by mass, respectively. Abbreviations: ALP, alkaline phosphatase; ARS, Alizarin red S; BMP-2, bone morphogenetic protein 2; BMSCs, bone marrow mesenchymal stem cells; NIR, near-infrared; OCN, osteocalcin; PTT, photothermal therapy; RUNX2, runt-related transcription factor 2; WB, Western blot.

thermal stimulation to amplify osteogenic signaling. This mechanism was further validated by Western blot analysis, in which the expression trends of BMP-2, RUNX2, ALP, and OCN were consistent with the ELISA results, with statistically significant upregulation in the 2BP+NIR group (Figure 4D and E). Taken together, these findings demonstrate that 2BP inherently possesses favorable osteogenic capacity and that its combination with NIR-induced mild PTT synergistically enhances osteogenesis through the upregulation of critical osteogenic proteins. This NIR-responsive osteogenic amplification effect highlights 2BP as a promising smart platform for controlled bone regeneration.

3.5. Osteogenic induction under an *in vitro* inflammatory microenvironment

The acute phase of bone injury is typically accompanied by a massive accumulation of pro-inflammatory factors, among which TNF-α and CD86 exert detrimental effects on bone regeneration by disrupting osteoblast differentiation, promoting osteoclast activation, and impairing matrix mineralization. Therefore, modulating the levels of these pro-inflammatory mediators represents a crucial yet often underappreciated strategy to facilitate early-stage bone healing. To address this issue, an *in vitro* model was established to mimic the early inflammatory microenvironment following bone defects, using LPS to induce post-traumatic inflammation, and to evaluate the osteogenic potential of 2BP under pathological conditions (Figure 5).

ALP staining (Figure 5A) and quantitative analysis (Figure 5D) revealed that LPS treatment significantly suppressed BMSC osteogenic differentiation, highlighting the inhibitory effect of excessive inflammation on bone formation. In contrast, 2BP partially reversed this LPS-induced impairment, as evidenced by increased ALP activity compared with the LPS-treated control group. Notably, NIR irradiation further potentiated the osteogenic capacity of 2BP, resulting in the highest ALP expression among all experimental groups and indicating a synergistic interaction between BP and mild photothermal stimulation in counteracting inflammatory inhibition. To elucidate the anti-inflammatory mechanisms underlying these observations, immunofluorescence staining was performed to assess the expression of CD86, a key marker of pro-inflammatory M1 macrophage polarization and a critical mediator of sustained inflammatory cascades.[30] To further analyze the anti-inflammatory mechanism of BP scaffolds and NIR irradiation, the scaffolds were co-cultured with RAW 264.7 cells induced by LPS. As shown in Figure 5B and F, CD86 expression was markedly downregulated in both the 2BP and 2BP+NIR groups, with the latter exhibiting the most pronounced reduction. This suggests that 2BP, particularly when combined with NIR irradiation, exerts robust anti-inflammatory effects by suppressing the expression of pro-inflammatory mediators. These findings were further validated by Western blot analysis (Figure 5C & E), which demonstrated decreased protein levels of both CD86 and TNF-α in the 2BP groups compared with the LPS-treated control. The 2BP+NIR group showed the lowest expression of these pro-inflammatory factors, confirming that NIR-induced mild PTT synergizes with BP to enhance anti-inflammatory efficacy. This synergism may arise from two complementary mechanisms: (i) accelerated BP degradation under NIR irradiation, releasing bioactive phosphorus species with inherent immunomodulatory properties; and (ii) mild thermal stimulation directly suppressing pro-inflammatory signaling pathways in BMSCs and infiltrating immune cells.

Collectively, these results indicate that 2BP possesses intrinsic anti-inflammatory properties, enabling it to partially reverse inflammation-mediated osteogenic inhibition. Under NIR irradiation, this dual functionality—attenuating excessive inflammation while promoting osteogenesis—is significantly enhanced, making 2BP a promising therapeutic platform for bone defect repair under pathological inflammatory conditions. This capacity to simultaneously modulate the inflammatory microenvironment and enhance osteogenic activity addresses a critical unmet need in bone tissue engineering scaffolds.

To further investigate the underlying mechanisms, RNA sequencing analysis was performed on cells from the 0BP and 2BP groups (Figure 6). As shown in Figure 6A, compared with the 0BP group, a total of 4775 genes were significantly upregulated and 2372 genes were significantly downregulated in the 2BP group. Among these DEGs, key regulators including *Hmox1*, *Grem1*, Sqstm1, *Egr1*, and *Irf9* were markedly upregulated (Figure 6B & E). *Hmox1* is a central gene in anti-inflammatory and antioxidant responses, exerting broad cytoprotective, anti-inflammatory, and immunomodulatory effects by degrading heme to produce carbon monoxide, biliverdin, and bilirubin. Furthermore, *Hmox1* promotes osteoblast differentiation, inhibits osteoclastogenesis, and facilitates bone repair.[31,32] *Grem1*, acting as a BMP antagonist, plays a pivotal role in skeletal development and homeostasis by precisely regulating the balance between osteogenesis and chondrogenesis.[33] *Sqstm1* is involved in autophagy and the nuclear factor erythroid 2-related factor 2–Kelch-like ECH-associated protein 1 signaling pathway and is crucial for maintaining osteoblast function; its deficiency

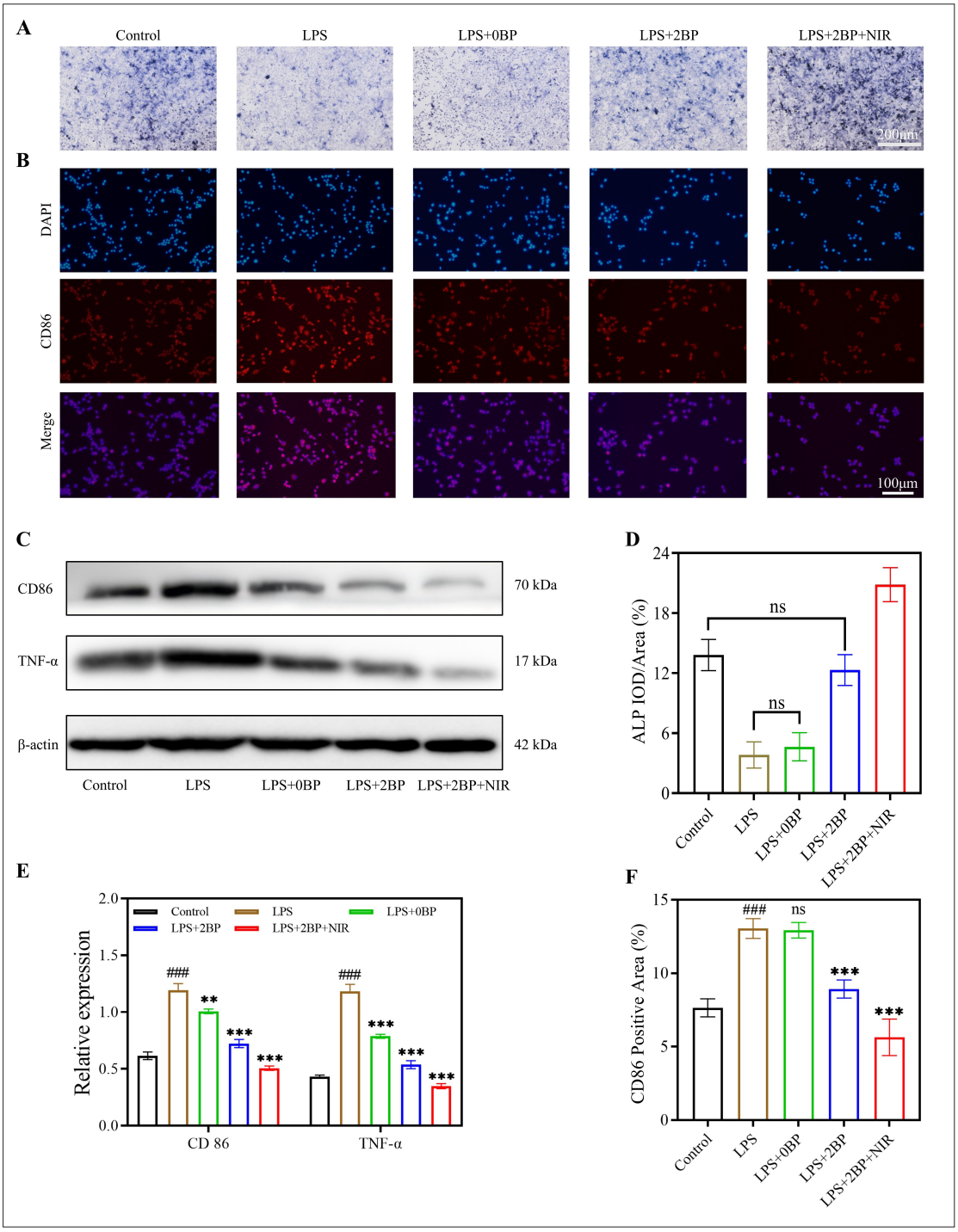

Figure 5. Osteogenic differentiation of BMSCs in an inflammatory microenvironment induced by macrophage-conditioned medium and secretion of inflammatory factors by RAW 264.7 cells under different culture conditions. (A) Alkaline phosphatase staining of BMSCs cultured in conditioned medium for 14 days. The osteogenic induction medium under inflammatory conditions for the control group was prepared by mixing RAW 264.7 culture medium (without additional intervention) and regular osteogenic induction medium at a 1:2 volume ratio (scale bar: 100 μm; magnification: 40×). (B) CD86 staining of LPS-incubated RAW 264.7 cells treated with different BP scaffolds for 48 h. (C) Pro-inflammatory protein expression (CD86, TNF-α) in LPS-incubated RAW 264.7 cells after co-culture with different BP scaffolds for 48 h. (D) Quantitative analysis of BMSCs cultured in conditioned medium for 14 days. (E) Relative protein expression levels. (F) Percentage of CD86-positive cells in different groups. Notes: NIR parameters: 808 nm, 0.8 W/cm^2, 5 min per day. $n = 6$, ns = $p > 0.05$, $^{###}p < 0.001$ vs. control group; $^{**}p < 0.01$ and $^{***}p < 0.001$ vs. LPS group. 0BP and 2BP represent scaffolds containing 0% and 2% BP by mass, respectively. Abbreviation: BMSCs, bone marrow mesenchymal stem cells; CD86, cluster of differentiation 86; DAPI, 4',6-diamidino-2-phenylindole; LPS, lipopolysaccharide; NIR, near-infrared; TNF-α, tumor necrosis factor α.

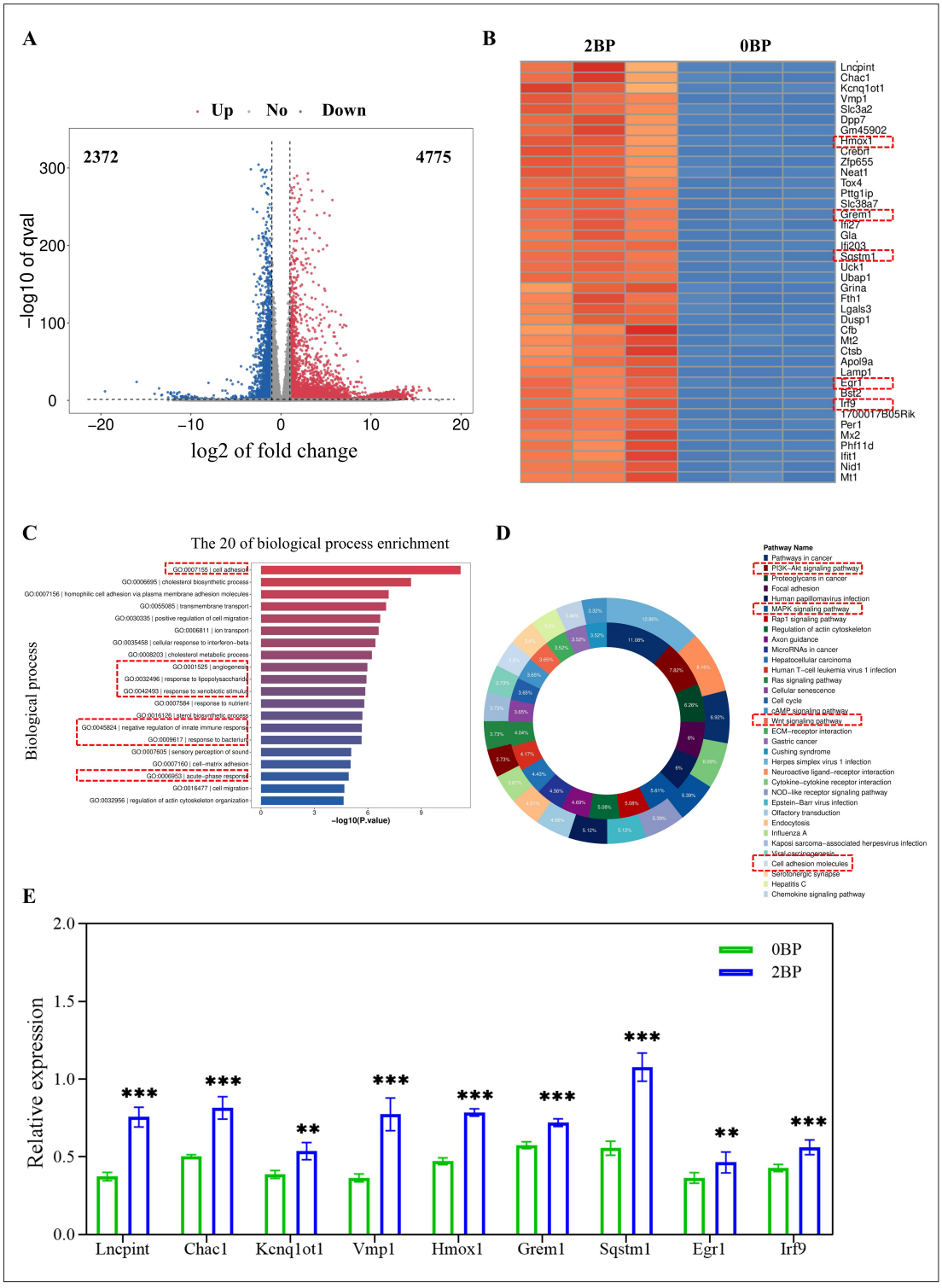

Figure 6. Sequencing results of cells from the 0BP and 2BP groups. (A) Volcano plot of DEGs; downregulated and upregulated genes are shown in blue and red, respectively. (B) Hierarchical clustering heatmap of DEGs. (C) Gene Ontology functional analysis and (D) Kyoto Encyclopedia of Genes and Genomes enrichment analysis of DEGs. (E) Relative expression levels of selected DEGs. $n = 6$; $^{**}p < 0.01$, $^{***}p < 0.001$. 0BP and 2BP represent scaffolds containing 0% and 2% BP by mass, respectively. Abbreviations: AKT, protein kinase B; cAMP, cyclic adenosine monophosphate; DEGs, differentially expressed genes; ECM, extracellular matrix; MAPK, mitogen-activated protein kinase; NOD, nucleotide-binding oligomerization domain-like; PI3K, phosphoinositide 3-kinase; Rap1, ras-proximate-1.

can lead to disrupted bone metabolism. Studies also indicate that *Sqstm1* can induce the expression of various anti-inflammatory genes, including *Hmox1*.[34–36] *Egr1* is a key transcription factor in mechanotransduction-induced osteogenesis, directly promoting the expression of osteogenic genes.[37] *Irf9*, a core component of the interferon signaling pathway, plays a dual role in immune regulation.[38] Collectively, the upregulation of these genes suggests that 2BP can promote the expression of genes associated with both osteogenesis and anti-inflammation. Gene Ontology enrichment analysis of the DEGs revealed several biological processes potentially linked to these effects (Figure 6C), including responses to xenobiotic stimulus, LPS, bacteria, and acute-phase response, all of which are closely associated with anti-inflammatory mechanisms. Conversely, processes such as angiogenesis, cell migration, positive regulation of cell migration, cell–matrix adhesion, and regulation of actin cytoskeleton organization are critically relevant to the proliferation, adhesion, and function of osteogenic cells. Kyoto Encyclopedia of Genes and Genomes pathway analysis further highlighted several signaling pathways that may mediate the osteogenic and anti-inflammatory properties of 2BP, including the phosphoinositide 3-kinase/protein kinase B, mitogen-activated protein kinase, and Wnt signaling pathways, which are well-established regulators of bone formation and inflammatory responses.[38–40] In summary, these transcriptomic findings indicate that the 2BP scaffold may exert its beneficial effects by activating key biological pathways related to osteogenesis and anti-inflammation.

3.6. Radiological evaluation of bone regeneration *in vivo* promoted by black phosphorus scaffolds

A rat model of distal femoral bone defect was established, and scaffolds were implanted into the defect area to evaluate their *in vivo* bone regeneration efficacy (Figure 7A). Figure 7B shows the scaffold (indicated by red arrows) implanted into the bone defect region (marked by green arrows). Infrared thermometry monitoring revealed that the femoral defect area of rats implanted with 2BP exhibited a gradual temperature increase under NIR irradiation, confirming that 2BP can mediate photothermal effects *in vivo* (Figure 7C and D). Specifically, 2BP generated moderate photothermal feedback *in vivo*: under 808 nm NIR irradiation at 1.2 W/cm^2, the local temperature increased significantly within 20 s and reached 41.1°C after 60 s, which falls within the optimal range for promoting osteogenesis without inducing thermal damage. These results further validate that a photothermal converter (i.e., BP) is an essential component for fabricating NIR-responsive scaffolds, as 0BP failed to exhibit measurable temperature elevation under identical conditions. Collectively, these data demonstrate that 2BP can generate mild photothermal effects *in vivo* upon external NIR stimulation, a property hypothesized to accelerate bone repair through thermally modulated cellular activities and enhanced tissue perfusion.

At 6 weeks post-implantation, micro-computed tomography was performed to assess bone regeneration in the defect area. As shown in Figure 7E, all scaffold groups exhibited new bone formation around the implant, with the formation of a regenerative bone bridge connecting the host bone and scaffold. Notably, the BP scaffold group showed a significantly thicker and denser bone bridge compared with the 0BP group, indicating that BP incorporation enhances bone repair. Among all groups, the 2BP+NIR group achieved the most extensive bone regeneration, with visible trabecular ingrowth into the scaffold pores, consistent with the *in vitro* findings of synergistic osteogenesis under photothermal stimulation. Interestingly, the 0BP+NIR group exhibited slightly improved bone repair compared with the 0BP group, despite the lack of significant differences in osteogenic markers observed *in vitro*. This *in vivo–in vitro* discrepancy may be attributed to the following: although 0BP cannot generate BP-mediated photothermal conversion, NIR irradiation may induce mild hyperthermia in the surrounding tissues through non-specific absorption, thereby improving local blood circulation and nutrient exchange—factors that play a more prominent role *in vivo* than in static *in vitro* cultures. However, this effect was relatively modest and did not reach statistical significance, reinforcing the necessity of BP as a specific photothermal agent for robust therapeutic efficacy. Quantitative analysis of new bone formation (Figure 7F) included trabecular thickness (μm), trabecular number (1/mm), bone mineral density (g/cm^2), and bone volume fraction (%). All parameters, which are well-recognized indicators of bone quality and regeneration extent, positively correlated with the qualitative repair outcomes: the 2BP+NIR group achieved the highest values, followed by the 2BP group, while the 0BP+NIR group showed a non-significant trend toward improved outcomes compared with the 0BP group.

In summary, 2BP exhibits excellent NIR responsiveness *in vivo*, and NIR irradiation significantly accelerates bone repair. Clinically, such efficient bone regeneration could mitigate repair failure caused by inter-individual heterogeneity, which remains a major challenge in current bone defect treatments. Furthermore, accelerated bone healing aligns with the principles of Enhanced Recovery After Surgery, which emphasize minimizing surgical trauma and promoting rapid functional recovery.[41] By

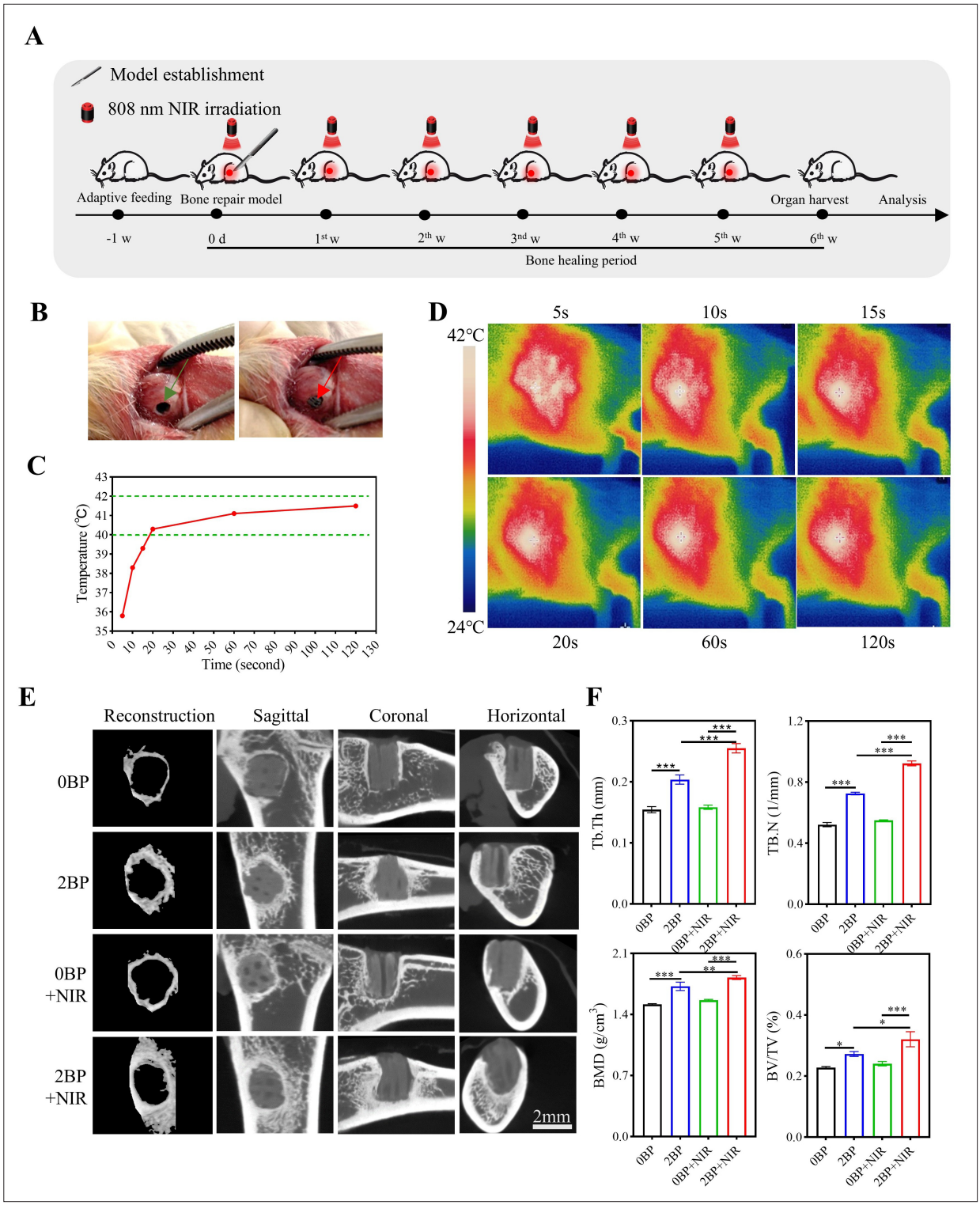

Figure 7. *In vivo* photothermal response properties of scaffolds and radiological evaluation of bone repair. (A) Flow chart of the animal experiment. (B) Scaffolds implantation process. Green arrow: bone defect area; red arrow: scaffold. (C) Temperature rise curves at different time points and (D) *in vivo* photothermal effect of 2BP at corresponding time points. (E) Qualitative micro-computed tomography images of bone repair in the distal femur of rats 6 weeks after surgery. (F) Quantitative analysis of bone repair. Notes: NIR parameters: 808 nm, 1.2 W/cm², 10 min per week. $n = 3$, $^{*}p < 0.05$, $^{**}p < 0.01$, $^{***}p < 0.001$. 0BP and 2BP represent scaffolds containing 0% and 2% BP by mass, respectively. Abbreviations: BMD, bone mineral density; BV/TV, bone volume/total volume; NIR, near-infrared; TB.N, trabecular number; Tb.Th, trabecular thickness.

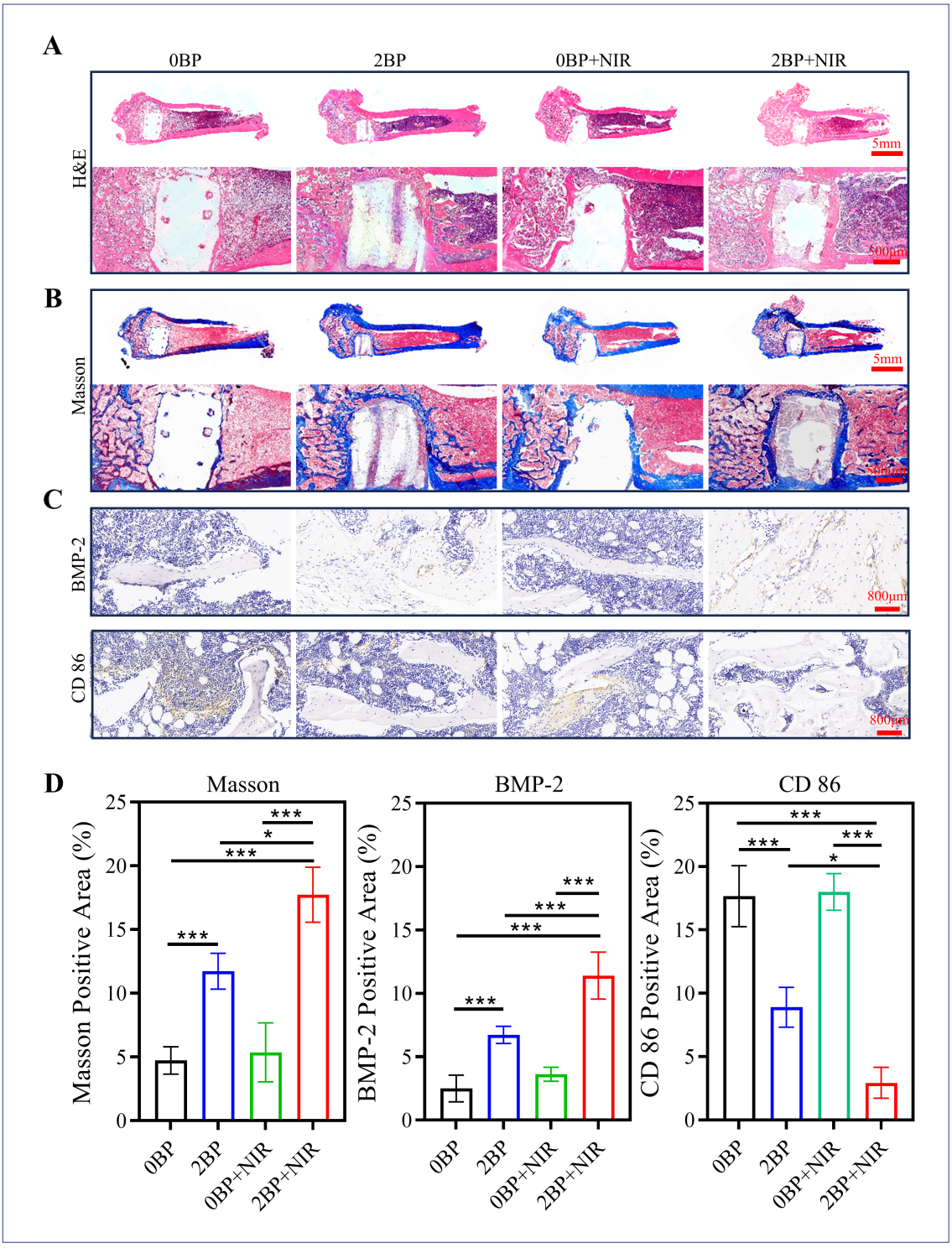

Figure 8. Bone tissue analysis for the bone defects of animals. (A) Hematoxylin and eosin (H&E) staining and (B) Masson's trichrome staining (scale bars: 5 mm [top row] and 500 μm [bottom row]; magnifications: 4× [top row] and 40×[bottom row]). (C) bone morphogenetic protein 2 (BMP-2) and cluster of differentiation 86 (CD86) staining (scale bar: 800 μm). (D) Corresponding relative positive area for Masson's trichrome, BMP-2, and CD86 staining. Notes: Near infrared (NIR) parameters: 808 nm, 1.2 W/cm^2, 10 min per week. $n = 3$, $^*p < 0.05$, $^{**}p < 0.01$, $^{***}p < 0.001$. 0BP and 2BP represent scaffolds containing 0% and 2% BP by mass, respectively.

enabling controlled photothermal stimulation to enhance regeneration, the 2BP holds promise for addressing unmet clinical needs in personalized bone defect therapy.

3.7. Histological evaluation of black phosphorus scaffolds for promoting bone regeneration *in vivo*

To further validate the bone repair efficacy of the scaffolds in defect areas, histological evaluations of peri-scaffold bone regeneration were performed. H&E staining and Masson's trichrome staining (Figure 8A & B) consistently demonstrated varying degrees of bone repair across all groups at 6 weeks post-implantation, with the 2BP+NIR group exhibiting the most robust regenerative outcomes. Specifically, this group showed dense trabecular bone formation, a thick and well-integrated bone repair bridge, and substantial new bone tissue within the defect area, indicating successful scaffold–host bone integration and progressive defect filling. BMP-2 is a key cytokine that directs BMSC differentiation into osteoblasts, promotes osteoblast maturation, and orchestrates bone remodeling, making it a critical mediator of *in vivo* bone repair. Immunohistochemical staining for BMP-2 and subsequent quantitative analysis (Figure 8C & D) were consistent with the histological repair patterns: the 2BP+NIR group displayed the highest BMP-2 expression, with statistically significant differences compared with other groups, confirming enhanced osteogenic signaling. In parallel, CD86 staining (Figure 8C & D) revealed that 2BP significantly suppressed local CD86 expression, with NIR irradiation further amplifying this anti-inflammatory effect to a statistically significant extent. These findings corroborate earlier *in vitro* observations, highlighting the scaffold's ability to modulate the inflammatory microenvironment *in vivo*, which is pivotal for establishing a favorable milieu for bone regeneration.

Collectively, these results confirm that 2BP outperforms conventional scaffolds (0BP) in promoting bone repair, likely through the dual mechanisms of upregulating pro-osteogenic factors and downregulating pro-inflammatory markers. Importantly, NIR irradiation synergistically enhances these effects, leading to significantly accelerated and more robust bone regeneration. Notably, sporadic cases of repair failure—characterized by scaffold loosening and lack of host bone integration—were observed in all groups except the 2BP+NIR group. This observation underscores a critical advantage of NIR-mediated photothermal stimulation: by enabling highly efficient bone regeneration, it mitigates the inter-individual heterogeneity in repair outcomes that often compromises conventional bone grafting strategies. Consequently, the 2BP+NIR approach holds promise for improving the overall success rate of bone defect repair, particularly in patient populations with limited regenerative capacity.

3.8. Biosafety evaluation of black phosphorus scaffolds *in vivo*

H&E staining (Figure S2) of major organs, including heart, liver, spleen, lungs, and kidneys, harvested from rats at week 6, revealed no pathological abnormalities. These results indicate that the BP scaffolds exhibit good biocompatibility and can be safely applied *in vivo*.

4. Conclusion

In this study, BP—a photothermal agent with excellent photothermal conversion efficiency—was incorporated into previously developed PLGA/β-TCP slurry to fabricate NIR-responsive BP scaffolds. These scaffolds were designed for bone defect repair by leveraging exogenous mild photothermal stimulation to enable PTT for accelerated bone regeneration. Structurally, the BP scaffolds mimicked cancellous bone architecture and were characterized by interconnected pores that facilitate nutrient exchange and cellular infiltration. Biologically, they exhibited superior biomineralization capacity, excellent biocompatibility, and non-cytotoxicity, as validated by *in vitro* cellular assays. The incorporation of BP endowed the scaffolds with robust NIR responsiveness, enabling on-demand, repeated, and controllable PTT interventions—a critical feature for personalized therapeutic regimens. Among the formulations tested, 2BP demonstrated optimal osteogenic and anti-inflammatory properties, making it particularly suitable for *in vivo* bone defect repair. These intrinsic functionalities were significantly potentiated under NIR irradiation, likely through synergistic mechanisms: (i) BP-mediated photothermal conversion generating mild hyperthermia (40–42°C) to enhance osteogenic signaling and modulate immune responses; (ii) accelerated BP degradation under NIR irradiation, leading to the release of bioactive phosphorus species that further promote mineralization and dampen inflammation. Notably, NIR-triggered PTT using 2BP represents a minimally invasive, spatiotemporally controllable intervention strategy that aligns with clinical needs for safe and efficient acceleration of bone repair. *In vivo* studies confirmed that the 2BP+NIR group achieved the highest bone repair success rate, with a reduced incidence of repair failure caused by inter-individual heterogeneity. This advantage is attributed to the scaffold's ability to override suboptimal regenerative microenvironments through controlled photothermal stimulation. Collectively, the NIR-responsive BP scaffold integrates multiple complementary functionalities, including structural mimicry, biocompatibility, osteogenesis promotion, anti-inflammatory effects, and controllable photothermal stimulation, to drive rapid bone defect repair. Its versatility and therapeutic efficacy position it as a promising candidate for clinical translation,

particularly in challenging scenarios such as large bone defects or bone repair in inflamed microenvironments.

Acknowledgments

None

Funding

This research was funded by the Eaglet Take-off Project of Jiangsu Provincial Association of Chinese Medicine (No. CYTF2024022) and the Feihong Plan of Nanjing TCM Hospital Affiliated to Nanjing University of Chinese Medicine (No. FHJH202405).

Conflict of interest

The authors declare that they have no known competing financial interests or personal relationships that could have influenced the work reported in this article.

Author contributions

Conceptualization: Chenjian Peng
Formal analysis: Peng Xue
Funding acquisition: Peng Xue
Investigation: Wei Zhang
Methodology: Anlong Liu, Chenjian Peng, Jun Wang
Project administration: Hongzhong Xi, Anlong Liu
Resources: Jianning Zhao
Software: Aoyun Hu
Supervision: Jianning Zhao
Validation: Hongzhong Xi, Wei Zhang, Jun Wang
Visualization: Aoyun Hu
Writing–original draft: Peng Xue
Writing–review & editing: Peng Xue, Hongzhong Xi

Ethics approval and consent to participate

This study was approved by the Ethics Committee of The Affiliated Hospital of Nanjing University (approval number: 2025 DW-002-01).

Consent for publication

Not applicable.

Availability of data

The data that support the findings of this study are available from the corresponding author upon reasonable request.

References

1. Wang J, Wu Y, Li G, *et al*. Engineering large-scale self-mineralizing bone organoids with bone matrix-inspired hydroxyapatite hybrid bioinks. *Adv Mater*. 2024;36(30):e2309875.
doi: 10.1002/adma.202309875

2. Chen H, Xi H, Guo M, *et al*. PLGA/β-TCP/ICT composite scaffold incorporating MXene (Ti3C2Tx) promotes osteogenesis through near-infrared-mediated mild photothermal therapy. *Mater Des*. 2024;244:113083.
doi: 10.1016/j.matdes.2024.113083

3. Chen H, Tan X, Fu J, *et al*. γ-Fe2O3/polydopamine/TiO2 nano-porous array composite coating (FPTCC) to modulate antibacterial, osteogenesis, and osseointegration through photothermal-magnetic response. *Mater Des*. 2024;248:113516.
doi: 10.1016/j.matdes.2024.113516

4. Hu X, Chen J, Yang S, *et al*. 3D printed multifunctional biomimetic bone scaffold combined with TP-Mg nanoparticles for the infectious bone defects repair. *Small*. 2024;20(40):e2403681.
doi: 10.1002/smll.202403681

5. Xie C, Ye J, Liang R, *et al*. Advanced strategies of biomimetic tissue-engineered grafts for bone regeneration. *Adv Healthc Mater*. 2021;10(14):e2100408.
doi: 10.1002/adhm.202100408

6. Huang Y, Wan X, Su Q, *et al*. Ultrasound-activated piezo-hot carriers trigger tandem catalysis coordinating cuproptosis-like bacterial death against implant infections. *Nat Commun*. 2024;15(1):1643.
doi: 10.1038/s41467-024-45619-y

7. Robin M, Mouloungui E, Castillo Dali G, *et al*. Mineralized collagen plywood contributes to bone autograft performance. *Nature*. 2024;636(8041):100-107.
doi: 10.1038/s41586-024-08208-z

8. Shen X, Zhang Z, Cheng C, *et al*. Bone regeneration and antibacterial properties of calcium-phosphorus coatings induced by gentamicin-loaded polydopamine on magnesium alloys. *Biomed Technol*. 2024;5:87-101.
doi: 10.1515/bmt-2023-0104

9. Liu X, Zhou J, Chen M, *et al*. 3D-printed biomimetic bone scaffold loaded with lyophilized concentrated growth factors promotes bone defect repair by regulation the VEGFR2/PI3K/AKT signaling pathway. *Int J Biol Macromol*. 2024;282(Pt 2):136938.
doi: 10.1016/j.ijbiomac.2024.136938

10. Liang W, Zhou C, Liu X, Pan B, Qian Y, Yang W. Current status of nano-embedded growth factors and stem cells delivery to bone for targeted repair and regeneration. *J Orthop Transl*. 2025;50:257-273.
doi: 10.1016/j.jot.2024.12.003

11. Zhao R, Han F, Yu Q, *et al*. A multifunctional scaffold that promotes the scaffold-tissue interface integration and rescues the ROS microenvironment for repair of annulus fibrosus defects. *Bioact Mater*. 2024;41:257-270.

doi: 10.1016/j.bioactmat.2024.06.025

12. Sun X, Gao Y, Li Z, He J, Wu Y. Magnetic responsive hydroxyapatite scaffold modulated macrophage polarization through PPAR/JAK-STAT signaling and enhanced fatty acid metabolism. *Biomaterials*. 2023;295: 122051.
doi: 10.1016/j.biomaterials.2023.122051

13. Xue P, Tan X, Xi H, *et al*. Low-temperature deposition 3D printing biotin-doped PLGA/β-TCP scaffold for repair of bone defects in osteonecrosis of femoral head. *IJB*. 2023;10(1):1152.
doi: 10.36922/ijb.1152

14. Xue P, Chen H, Xi H, *et al*. Magnesium dopped calcium-fluoride/icaritin composite multi-layer coating functionalized 3D printed β-TCP scaffold induces sustained bone regeneration in a rabbit model. *Mater Des*. 2022;223:111156.
doi: 10.1016/j.matdes.2022.111156

15. Sun H, Xu J, Wang Y, *et al*. Bone microenvironment regulative hydrogels with ROS scavenging and prolonged oxygen-generating for enhancing bone repair. *Bioact Mater*. 2023;24:477-496.
doi: 10.1016/j.bioactmat.2022.12.021

16. Yang X, Yang X, Luo P, *et al*. Novel one-pot strategy for fabrication of a pH-responsive bone-targeted drug self-frame delivery system for treatment of osteoporosis. *Mater Today Bio*. 2023;20:100688.
doi: 10.1016/j.mtbio.2023.100688

17. Xue P, Xi H, Chen H, He S, Liu X, Du B. Predictive value of clinical features and CT radiomics in the efficacy of hip preservation surgery with fibula allograft. *J Orthop Surg Res*. 2023;18(1):940.
doi: 10.1186/s13018-023-04431-y

18. Chen H, Xue P, Xi H, *et al*. A deep-learning model for predicting the efficacy of non-vascularized fibular grafting using digital radiography. *Acad Radiol*. 2024;31(4):1501-1507.
doi: 10.1016/j.acra.2023.10.023

19. Chen H, Xue P, Xi H, *et al*. Predicting efficacy and guiding procedure choice in non-vascularized bone grafting: a CT radiomics and clinical predictor approach. *BMC Musculoskelet Disord*. 2023;24(1):959.
doi: 10.1186/s12891-023-07095-1

20. Couce ML, Saenz de Pipaon M. Bone mineralization and calcium phosphorus metabolism. *Nutrients*. 2021;13(11):3692.
doi: 10.3390/nu13113692

21. Hou J, Yin S, Jiao R, *et al*. The combination of hydrogels and rutin-loaded black phosphorus nanosheets treats rheumatoid arthritis. *Mater Today Bio*. 2024;29:101264.
doi: 10.1016/j.mtbio.2024.101264

22. Huang S, Xu S, Hu Y, *et al*. Preparation of NIR-responsive, ROS-generating and antibacterial black phosphorus quantum dots for promoting the MRSA-infected wound healing in diabetic rats. *Acta Biomater*. 2022;137:199-217.
doi: 10.1016/j.actbio.2021.10.008

23. Wang W, Zhang G, Wang Y, *et al*. An injectable and thermosensitive hydrogel with nano-aided NIR-II phototherapeutic and chemical effects for periodontal antibacteria and bone regeneration. *J Nanobiotechnology*. 2023;21(1):367.
doi: 10.1186/s12951-023-02124-6

24. Wang M, Lu X, Yin X, *et al*. Synchrotron radiation-based Fourier-transform infrared spectromicroscopy for characterization of the protein/peptide distribution in single microspheres. *Acta Pharm Sin B*. 2015;5(3):270-276.
doi: 10.1016/j.apsb.2015.03.008

25. Zairani NAS, Jaafar M, Ahmad N, Abdul Razak K. Fabrication and characterization of porous β-tricalcium phosphate scaffolds coated with alginate. *Ceram Int*. 2016;42(4):5141-5147.
doi: 10.1016/j.ceramint.2015.12.034

26. Kang KR, Piao ZG, Kim JS, *et al*. Synthesis and characterization of β-tricalcium phosphate derived from *Haliotis* sp. shells. *Implant Dent*. 2017;26(3):378-387.
doi: 10.1097/ID.0000000000000559

27. Ma S, Wei Y, Sun R, *et al*. Calcium phosphate bone cements incorporated with black phosphorus nanosheets enhanced osteogenesis. *ACS Biomater Sci Eng*. 2023;9(1):292-302.
doi: 10.1021/acsbiomaterials.2c00742

28. Xue P, Chang Z, Chen H, *et al*. Macrophage membrane (MMs) camouflaged near-infrared (NIR) responsive bone defect area targeting nanocarrier delivery system (BTNDS) for rapid repair: promoting osteogenesis via phototherapy and modulating immunity. *J Nanobiotechnology*. 2024;22(1):87.
doi: 10.1186/s12951-024-02351-5

29. Shen G, Ren H, Shang Q, *et al*. Foxf1 knockdown promotes BMSC osteogenesis in part by activating the Wnt/β-catenin signalling pathway and prevents ovariectomy-induced bone loss. *EBioMedicine*. 2020;52:102626.
doi: 10.1016/j.ebiom.2020.102626

30. Kennedy A, Waters E, Rowshanravan B, *et al*. Differences in CD80 and CD86 transendocytosis reveal CD86 as a key target for CTLA-4 immune regulation. *Nat Immunol*. 2022;23(9):1365-1378.
doi: 10.1038/s41590-022-01289-w

31. He R, Wang Z, Cui M, *et al*. HIF1A alleviates compression-induced apoptosis of nucleus pulposus derived stem cells via upregulating autophagy. *Autophagy*. 2021;17(11): 3338-3360.
doi: 10.1080/15548627.2021.1872227

32. Hu L, Yu Y, Shen Y, *et al*. Ythdf2 promotes pulmonary hypertension by suppressing Hmox1-dependent anti-inflammatory and antioxidant function in alveolar macrophages. *Redox Biol*. 2023;61:102638.

doi: 10.1016/j.redox.2023.102638

33. Ng JQ, Jafarov TH, Little CB, *et al*. Loss of Grem1-lineage chondrogenic progenitor cells causes osteoarthritis. *Nat Commun*. 2023;14(1):6909. doi: 10.1038/s41467-023-42199-1

34. Agas D, Gabai V, Sufianov AA, Shneider A, Sabbieti MG. P62/SQSTM1 enhances osteogenesis and attenuates inflammatory signals in bone marrow microenvironment. *Gen Comp Endocrinol*. 2022;320:114009. doi: 10.1016/j.ygcen.2022.114009

35. Tang D, Kang R. SQSTM1 is a therapeutic target for infection and sterile inflammation. *Cytokine*. 2023;169: 156317. doi: 10.1016/j.cytokine.2023.156317

36. Lingli Z, Xing H, Liqiu W, *et al*. Palmitoylation restricts SQSTM1/p62-mediated autophagic degradation of NOD2 to modulate inflammation. *Cell Death Differ*. 2022;29(8):1541-1551. doi: 10.1038/s41418-022-00942-z

37. Li Y, Lu D, Xu F, *et al*. EGR1 promotes craniofacial bone regeneration via activation of ALPL^{+}PDGFD^{+} periosteal stem cells. *Adv Sci (Weinh)*. 2025;12(30):e10243. doi: 10.1002/advs.202410243

38. Zhang H, Cai D, Bai X. Macrophages regulate the progression of osteoarthritis. *Osteoarthritis Cartilage*. 2020;28(5):555-561. doi: 10.1016/j.joca.2020.01.007

39. Wang J, Zhang Y, Cao J, *et al*. The role of autophagy in bone metabolism and clinical significance. *Autophagy*. 2023;19(9):2409-2427. doi: 10.1080/15548627.2023.2186112

40. Katz JN, Arant KR, Loeser RF. Diagnosis and treatment of hip and knee osteoarthritis: a review. *JAMA*. 2021;325(6):568-578. doi: 10.1001/jama.2020.22171

41. Xie C, Liang R, Ye J, *et al*. High-efficient engineering of osteo-callus organoids for rapid bone regeneration within one month. *Biomaterials*. 2022;288:121741. doi: 10.1016/j.biomaterials.2022.121741